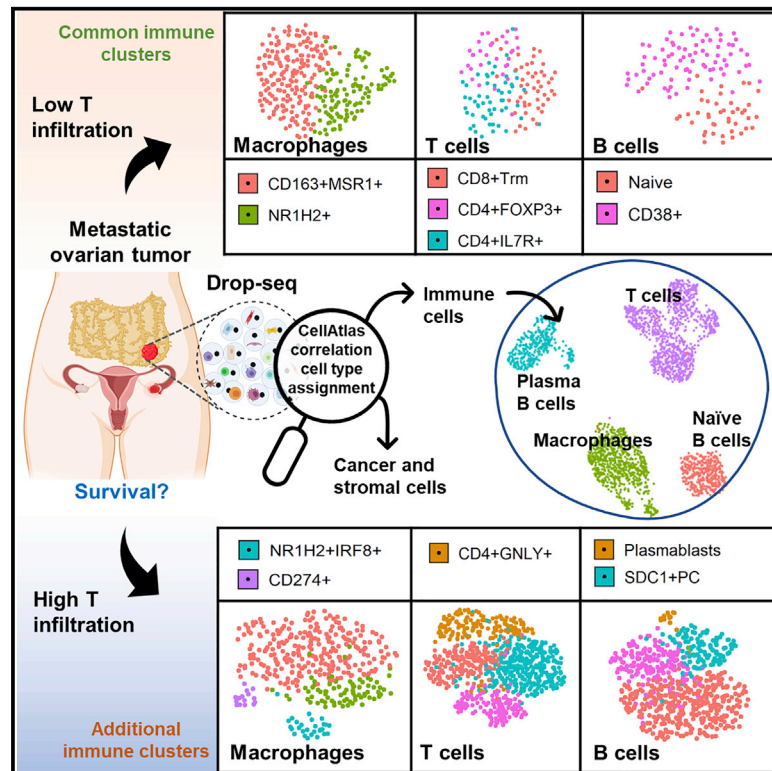


Characterizing the tumor microenvironment of metastatic ovarian cancer by single-cell transcriptomics

Graphical abstract



Authors

Susan Olalekan, Bingqing Xie, Rebecca Back, Heather Eckart, Anindita Basu

Correspondence

solalekan@uchicago.edu (S.O.),
onibas@uchicago.edu (A.B.)

In brief

Although molecular subtypes of ovarian cancer have been established from bulk-RNA sequencing, single-cell resolution is critical for developing personalized immunotherapies. Using Drop-seq data of single cells from ovarian tumors resected from omental metastases, Olalekan et al. reveal immune cell types and subsets with possible roles in the management of disease.

Highlights

- Ovarian tumors separate into two groups: high T and low T cell infiltration groups
- *Granulysin*-expressing CD4⁺ T cells are present in the high T infiltration cell group
- MKI67-expressing plasmablasts are identified in high T cell infiltration tumors
- Correlation of *CD8* and *Tox* in this study with immunoreactive subtype in TCGA data



Article

Characterizing the tumor microenvironment of metastatic ovarian cancer by single-cell transcriptomics

Susan Olalekan,^{1,*} Bingqing Xie,¹ Rebecca Back,¹ Heather Eckart,¹ and Anindita Basu^{1,2,*}¹Section of Genetic Medicine, Department of Medicine, University of Chicago, 5841 S. Maryland Avenue, Chicago, IL 60637, USA²Lead contact*Correspondence: solalekan@uchicago.edu (S.O.), onibasus@uchicago.edu (A.B.)<https://doi.org/10.1016/j.celrep.2021.109165>**SUMMARY**

Understanding the cellular composition of the tumor microenvironment and the interactions of the cells is essential to the development of successful immunotherapies in cancer. We perform single-cell RNA sequencing (scRNA-seq) of 9,885 cells isolated from the omentum in 6 patients with ovarian cancer and identify 9 major cell types, including cancer, stromal, and immune cells. Transcriptional analysis of immune cells stratifies our patient samples into 2 groups: (1) high T cell infiltration (high T_{inf}) and (2) low T cell infiltration (low T_{inf}). *TOX*-expressing resident memory $CD8^+$ T ($CD8^+$ Trm) and granulysin-expressing $CD4^+$ T cell clusters are enriched in the high T_{inf} group. Concurrently, we find unique plasmablast and plasma B cell clusters, and finally, $NR1H2^+IRF8^+$ and $CD274^+$ macrophage clusters, suggesting an anti-tumor response in the high T_{inf} group. Our scRNA-seq study of metastatic tumor samples provides important insights in elucidating the immune response within ovarian tumors.

INTRODUCTION

Ovarian cancer is the most lethal malignancy of the female reproductive tract (Siegel et al., 2017). Conventional therapy involving cytoreductive surgery and chemotherapy is 90% effective when cancer is diagnosed at the early stage, when it is still restricted to 1 or both ovaries. Unfortunately, most ovarian cancer cases are diagnosed at stage III or IV, when the cancer has metastasized and the diagnosis in these patients results in a 30% 5-year survival rate (Testa et al., 2018). To develop efficacious therapies for metastatic ovarian cancer, we need to define the cellular heterogeneity and the transcriptional state within the tumor microenvironment. Immunohistochemical staining and flow cytometry have been useful in categorizing the cell types based on specific cell surface markers but mask intra-cellular heterogeneity. Bulk RNA profiling has been used to categorize high-grade serous ovarian carcinoma (HGSOC), the most common and lethal histotype of ovarian cancer, into molecular subtypes (Tothill et al., 2008; The Cancer Genome Atlas Research Network, 2011). However, bulk RNA sequencing (RNA-seq) averages gene expression and fails to identify the respective contribution of cell subsets. Single-cell RNA-seq (scRNA-seq) has emerged as a powerful tool to interrogate tumor composition, revealing cellular heterogeneity and gene regulatory networks at single-cell resolution (Zheng et al., 2017b; Villani et al., 2017; Dixit et al., 2016; Jaitin et al., 2016; Shalek et al., 2013; Zheng et al., 2017a). Recently, a scRNA-seq study investigated the heterogeneity in the proposed cell of origin of HGSOC and revealed a high epithelial-mesenchymal transition (EMT) prominent subtype

associated with poor prognosis (Hu et al., 2020). So far, transcriptomic studies in ovarian cancer have focused on cancer cells. However, the tumor microenvironment contains other cell types that are relevant to patient stratification, targeted treatment, and outcomes.

The omentum is a common metastatic site for peritoneal malignancies, including ovarian cancer (Krist et al., 1998). It is mainly an adipose tissue that contains aggregates of immune cells in areas called milky spots (Platell et al., 2000). These milky spots act similar to lymph nodes, collecting and responding to antigen within the peritoneal cavity. Interestingly, ovarian cancer cells preferentially colonize adipose tissue with milky spots in the peritoneal cavity (Clark et al., 2013). In addition, adipocytes provide adipokines and act as a source of energy for ovarian cancer cells (Nieman et al., 2011). These factors prime the omentum as a pre-metastatic niche for ovarian cancer. The initial presence of ovarian cancer cells in the omentum leads to a recruitment of macrophages into the milky spots without anti-tumor effects. Contrastingly, the presence of tumor-infiltrating $CD8^+$ T cells in both the ovary and omentum is associated with significantly longer overall survival (Santoiemma and Powell, 2015). However, checkpoint inhibitors, a cancer immunotherapeutic approach, aimed at restoring $CD8^+$ T cell function have had a low response rate in ovarian cancer patients (Santoiemma and Powell, 2015). We therefore need a better understanding of the tumor microenvironment to improve patient response to cancer immunotherapy.

In the present study, we use Drop-seq, a high-throughput single scRNA-seq technique to examine the cells within omental tumors from 6 patients with different pathology-graded histotypes



Table 1. De-identified metadata for metastatic omental tumors from 6 ovarian cancer patients

Patient ID	Age, y	Race	Origin	Histologic type	Histological grade	Neoadjuvant therapy	Stage (PMN/FIGO)
PT-1	62	white	undetermined	serous	not applicable	yes	ypT3a Nx M1/IVb
PT-2	56	white	left ovary	high grade serous carcinoma	high grade	no	pT3c Nx Mx/IIIc
PT-3	66	Black	left fallopian (STIC)	high grade serous carcinoma	high grade	yes	ypT3c N1a/IIIc
PT-4	46	Asian	left fallopian (STIC)	high grade serous carcinoma	high grade	no	pT3c Nx/IIIc
PT-5	71	Black	left fallopian (STIC)	high grade serous carcinoma	high grade	yes	pT3c, N1, M1/IIIc
PT-6	66	Asian	fallopian	malignant mixed Mullerian tumor	high grade	yes	ypT3c Nx/IIIc

of ovarian cancer. We identified 12 cell clusters among the patient cell population and stratified the patient samples into 2 groups based on immune signatures: (1) a high T cell infiltration (high T_{inf}) group, and (2) a low T cell infiltration (low T_{inf}) group. We also identified macrophage and B cell subsets that were unique to the high T_{inf} group. This concurrent single-cell transcriptomic analysis of solid metastatic ovarian cancer tumors unravels the genetic signatures of immune cell subsets within ovarian tumors and can guide future immunotherapeutic approaches.

RESULTS

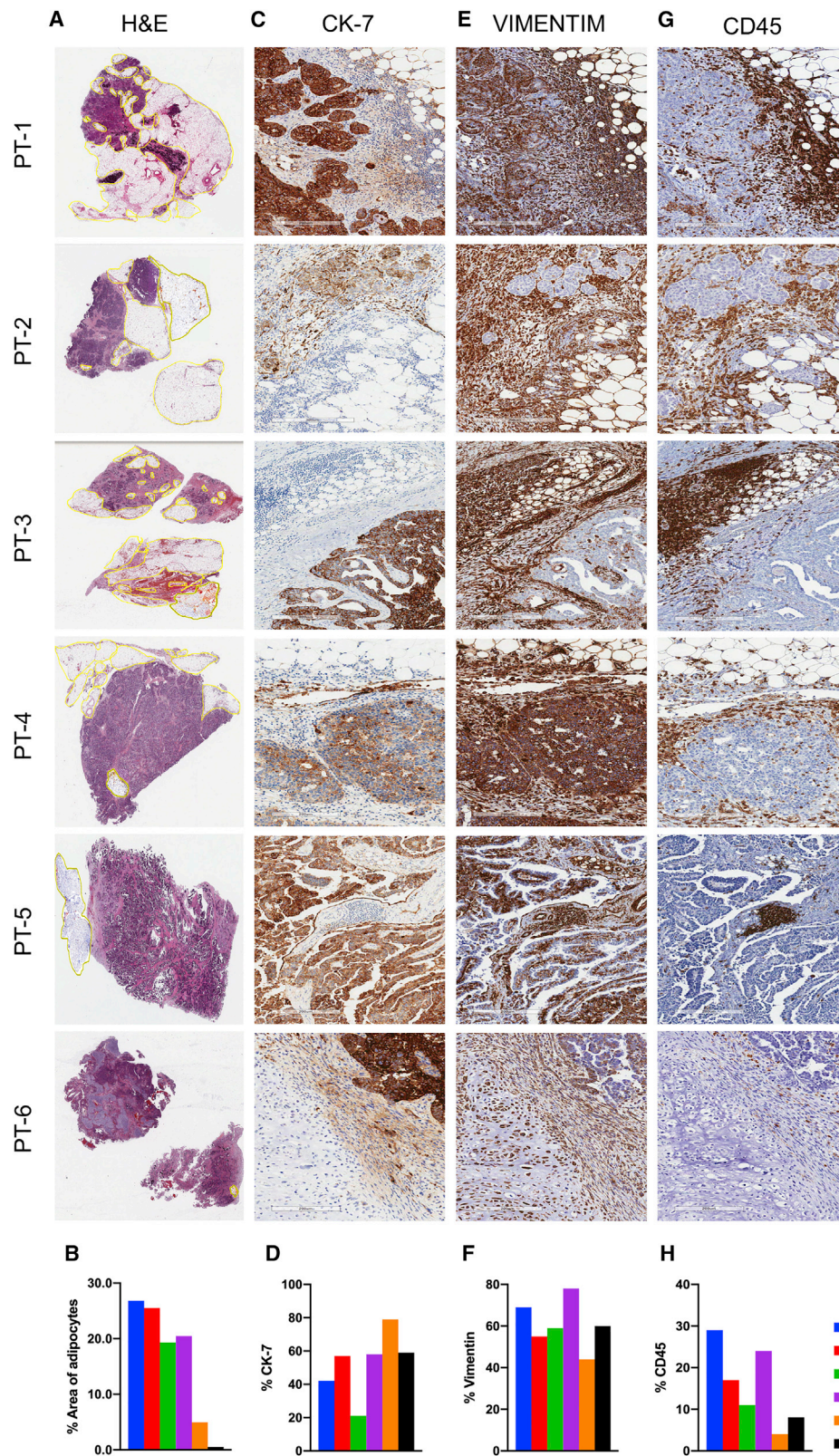
Characteristics of the tumor microenvironment

Ovarian cancer samples were collected from the omental metastatic site of 6 patients (Table 1). Four patients were diagnosed with advanced HGSOC, 1 with serous carcinoma, and 1 with malignant mixed Mullerian tumor (MMMT). The ages of the patients ranged from 46 to 71 years. Four of the patients received neo-adjuvant therapy before surgery, including the patient diagnosed with MMMT. As metastasis progresses, there is an inverse relationship between ovarian tumor growth (cancer and cancer-associated cell growth) and adipocytes within the omentum (Nieman et al., 2011). Therefore, the area of tumor occupied by adipocytes decreases with disease score (Pearce et al., 2018). The area of adipocytes shown using hematoxylin and eosin (H&E)-stained sections (Figure 1A) was reported as a percentage of the total surface area of the samples and used as a measure of disease score (Figure 1B), similar to Pearce et al. (2018). We rated the patient samples from lowest to highest disease score: PT-1–PT-6, respectively. The percentages of cancer cells, stromal cells, and immune cells were quantified by immunohistochemistry (IHC) using antibodies against cytokeratin-7 (CK-7), vimentin, and CD45, respectively (Figures 1C–1H). There was a varying proportion of each cell type across patients. Notably, we observed that malignant cells in some patients (PT-1, PT-4, PT-5, and PT-6) double stained for CK-7 and vimentin, suggesting active EMT (Figures 1C–1F). In addition, the MMMT (PT-6) sample had 2 different types of malignant cells that stained separately for CK-7 and vimentin. We assessed the relationship between the area of adipocytes and the cancer and stromal compartments and observed a positive correlation with CD45⁺ immune cells, suggesting that the less transformed the omental tissue, the higher the CD45⁺ immune cells observed (Figure S1). We also observed aggregation of immune cells closer to adipocytes and sparsely otherwise throughout the rest of the tissue.

These data reveal patient variability in the cellular transformation of tumors in the late pathological stage.

Generation of single-cell data, cell clustering, and cell-type assignment

For Drop-seq experiments, each tumor sample was enzymatically digested into a single-cell suspension and processed (Macosko et al., 2015). We integrated all 6 omental samples into a gene expression matrix that contains the expression values of 9,885 cells and 40,947 genetic features such as protein coding genes, pseudogenes, and long non-coding RNA (lncRNA), mapped from the GENCODE (version GRCh38). Cells from all of the patient samples had an average of 4,296 unique molecular identifiers (UMIs), 1,742 genes, and 7.8% UMI counts of mitochondrial origin per cell, as shown in Table 2. A minimum cutoff of 600 genes per cell was set. Hierarchical clustering was performed using a resolution of 0.2, with 12 clusters detected (Figure 2A). Cells from each patient were present in the major clusters (Figure S2; Table S1). The cell types were assigned and curated using cell line correlation, canonical genes, and functional categories according to significantly differentially expressed genes from the detected clusters. We were able to identify and assign a cell type to 9 major clusters with or without the MMMT sample (Figures 2A and S2). This included 1 cluster each for epithelial cells, fibroblasts, mesenchymal stem cells (MSCs), embryonic stem cells (ESCs), endothelial cells, and 4 clusters of immune cells. Three remaining unidentified clusters, marked N1, N2, N3, contained relatively few cells (<60) and lacked confidence in the identification of these cell types. Each patient sample had a varying proportion of cells in the 9 identified cell types/clusters (Figure 2B). Previous bulk mRNA and microRNA expression studies have established 4 molecular subtypes of HGSOC (The Cancer Genome Atlas Research Network, 2011; Tothill et al., 2008). To assign molecular subtypes to our samples, we extracted gene sets defining each ovarian cancer molecular subtype using The Cancer Genome Atlas (TCGA) data (The Cancer Genome Atlas Research Network, 2011) and applied them to our Drop-seq data. We found that all 4 molecular subtypes are represented in each patient tumor sample, including the MMMT sample (Figure 2C). We further analyzed which cell type/cluster belonged to each molecular subtype. The differentiated and proliferative subtypes mainly consisted of epithelial cells. The immunoreactive subtype contained a high ratio of immune cells. The low ratio of epithelial cells in the immunoreactive subtype suggests that these tumors may be proliferative or differentiated tumors with an immune response. The



(legend on next page)

Table 2. Statistics and filter parameters applied to samples collected from 6 patients and the resulting number of cells, genes, and UMI per sample

Patient ID	Raw reads	Gene cutoff	No. genes	No. cells	Mean no. genes per cell	Median no. genes per cell	Mean no. UMIs per cell	Median no. UMIs per cell
PT-1	60,870,530	600	24,776	1,244	1,517	979	4,229	1,940
PT-2	308,036,080	800	32,024	3,451	1,894	1,391	4,802	2,796
PT-3	56,498,174	800	24,063	1,071	1,625	1,308	3,849	2,728
PT-4	144,287,737	700	19,297	1,102	1,830	1,391	5,235	3,034
PT-5	89,967,519	700	26,499	1,108	1,744	1,313	3,795	2,332
PT-6	77,505,171	800	26,221	1,909	1,624	1,387	3,425	2,595

mesenchymal subtype is very different from the other subtypes, consisting of a high ratio of fibroblasts. These findings are consistent with a recent study from Schwede et al. (2020) that examined bulk mRNA-seq TCGA data and reported that ovarian cancer molecular subtypes reflect the proportion of cell types within each tumor (Figure 2D).

We wanted to test whether the established molecular subtypes could be useful in specifically categorizing cancer cells within a tumor. However, most of the epithelial cells belonged to the differentiated, proliferative, and undecided subtypes (Figure 2D). Based on the expression of *WT1* and *CD24*, we refer to this cluster as “cancer epithelial cells” (Figure S2) (Hylander et al., 2006; Kristiansen et al., 2002). We also integrated our data with previously published ovarian cancer scRNA-seq data, and all of the cancer epithelial cells were co-localized (data not shown) (Shih et al., 2018; Izar et al., 2020). The chondrosarcomatous elements of MMMT (PT-6) were confirmed by our Drop-seq data (Figure S2; Table S1). Next, we extracted cells from the central cluster, cancer epithelial cells, and ESCs that cluster closely together and performed hierarchical clustering. A total of 7 clusters were detected (Figure 2E, top). The heatmap of the top 10 differentially expressed genes based on adjusted p value for all subclusters are shown in Figure 2E (bottom). The top processes as revealed by Gene Ontology analysis are epithelial tube morphogenesis (cluster 2), epithelial cell differentiation (clusters 3 and 5), and epithelial cell proliferation (cluster 6) (Table S2). Epithelial ovarian cancer was the top disease for clusters 1, 3, and 6 (Table S2). Some previously described marker genes that differentiate the subclusters are shown (Figure 2F and Table S3). *PAX8* and *MUC16*, indicative of advanced disease, were expressed by cluster 2 (adjusted $p = 4.95 \times 10^{-13}$ and 1.83×10^{-53}) (Robertson et al., 1999; Thériault et al., 2011). *MUC16* was also expressed by cluster 3 (adjusted $p = 2.86 \times 10^{-6}$). Clusters 1 and 6 expressed both *MKI67* (adjusted $p = 3.5 \times 10^{-168}$ and 4.19×10^{-31}) and *VIM* (adjusted $p = 0.01$ and 3.92×10^{-32}), indicative of a proliferating population. Cluster 5 expressed *FN1* (adjusted $p = 0.05$) and *ZEB1* (adjusted $p = 0.01$),

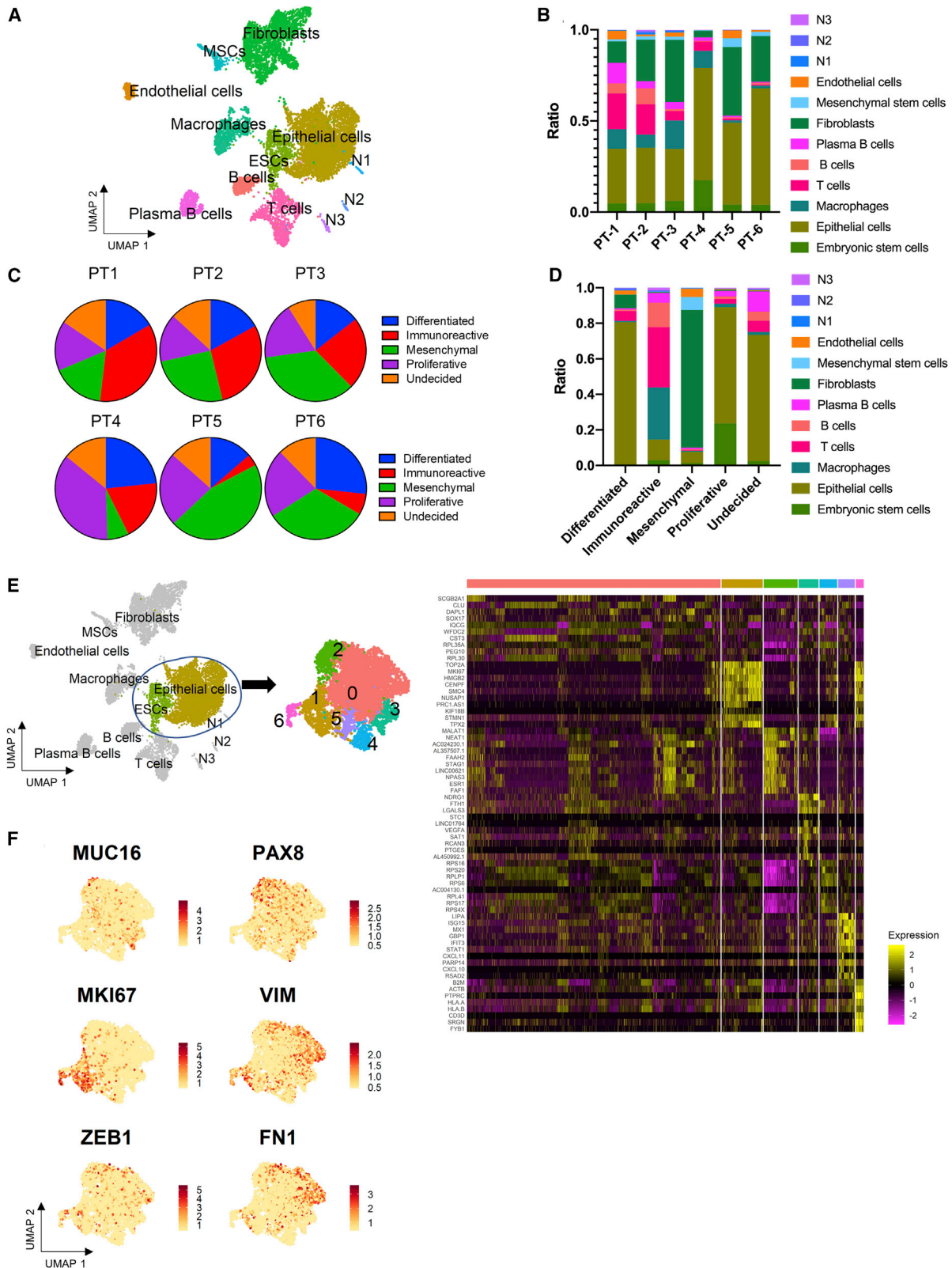
markers of EMT. Ovarian cancer stem cells, marked by the co-expression of *CD33*, *CD44*, *CD117*, and *CD24*, were not observed (Klemba et al., 2018). These results reveal a snapshot of the heterogeneous transcriptional state of cancer cells during the later course of disease (International Federation of Gynecology and Obstetrics [FIGO] stages IIIc–IVb).

Immune cellular profile of patient samples

To investigate the immune population in our patient samples, we performed clustering on the immune cells from the 6 patient samples; the cells clustered into 4 main populations: T cells, B cells, plasma B cells, and macrophages (Figure 3A). Using a dendrogram to group samples with similar cell populations, our cohort was separated into 2 groups based on their T cell population: (1) the high T cell infiltration (high T_{inf}) group (PT-1 and PT-2) and (2) low T_{inf} group (PT-3–PT-6) (Figure 3B). Interestingly, the high T_{inf} group had the lowest disease scores (as determined by IHC; Figure 1), while the low T_{inf} group showed relatively higher disease scores. The results are consistent with and without the MMMT sample (Figures 3B and S2); the MMMT sample (PT-6) belongs to the low T_{inf} group (Figure 3B). Macrophages are recruited from the peritoneal cavity during the initial phase of metastasis (Shimotsuma et al., 1992; Oosterling et al., 2006). The presence of M1 ($CD68^+$) and M2 ($CD163^+$) macrophages were confirmed by IHC staining (Figure S3). To assess the differences in the macrophage population, we performed unsupervised clustering separately on macrophages from the high T_{inf} group and low T_{inf} group, respectively (Figures 3C and 3D). Both groups had a $CD163^+CD204^+$ cluster that also highly expressed *CD14* and *FCGR3A* reminiscent of tumor-associated macrophages (TAMs) (Figures 3E, 3F, and S4; Table S4). Closely associated with this cluster is the $NR1H2^+$ cluster that is present in both high T_{inf} and low T_{inf} group. *NR1H2* inhibits inflammatory genes in macrophages (Castrillo et al., 2003; A-González and Castrillo, 2011). The high T_{inf} group also included a $NR1H2^+$ sub-cluster that expresses *IRF8*⁺ (adjusted $p = 2.1 \times 10^{-8}$). *IRF8* is induced in the presence of *IFNG* and promotes the formation

Figure 1. Immunohistochemical staining and sample description

(A and B) Hematoxylin and eosin (H&E)-stained sections (A) with (B) the histogram of the percentage area of adipocytes in the patient samples. (C and D) Cytokeratin-7 (CK-7) staining on patient samples (C) with (D) the histogram of the percentage of CK-7⁺ cells. (E and F) Vimentin staining on patient samples (E) with (F) the histogram of percentage of vimentin-positive cells. (G and H) CD45 staining on patient samples (G) with (H) the histogram of the percentage of CD45⁺ cells. Images were taken at (A) 40 \times , and (C, E, and G) 400 \times .



(legend on next page)

of autophagosomes (Figures 3E, 3F, and S4) (Gupta et al., 2015). Finally, the high T_{inf} group included a $CD274^+$ cluster, suggesting a regulatory population similar to myeloid-derived suppressor cells (MDSCs). However, these $CD274^+$ cells also express $CCR7$ (adjusted $p = 4.1 \times 10^{-8}$), a marker for M1 macrophages that are positively associated with survival time in cancer (Yuan et al., 2015; Ma et al., 2010). Both $NR1H2^+IRF8^+$ and $CD274^+$ clusters express $FLT3$. $FLT3^+$ progenitors can differentiate into osteoclasts, dendritic cells, microglia, and macrophages (Servet-Delprat et al., 2002). The $CD274^+$ cluster also expressed $ZBTB46$ and $CD80$ (Figures 3G and 3H). There is a positive Pearson correlation (Table S4) between these markers, suggesting that the $CD274^+$ cluster is similar to M1 macrophages. We assessed cluster N3 in our dataset, which closely resembles dendritic cells, albeit the few number of cells detected, for genes expressed by macrophages. The N3 cluster (dendritic cells), mainly found in the high T_{inf} group (Figure S2; Table S1), also expressed $IRF8$, $FLT3$, and $HLA.DRA$ (Figure S4). This analysis reveals transcriptionally distinct macrophages present in tumors, in addition to the presence of established TAMs.

Differences in T cell clustering and subtype analysis

To reveal the functional subtypes of T cells and differences in the high T_{inf} versus low T_{inf} groups, we clustered 820 and 136 T cells, respectively (Figures 4A and 4B). To enable a fair comparison between the 2 disease groups, we randomly subsampled the T cells within the high T_{inf} group to match the T cell numbers in the low T_{inf} group. The subsampling was performed 50 times for statistical confidence and the number of T cell clusters in each group remained the same (data not shown).

A total of 4 and 3 transcriptionally distinct clusters emerged from high T_{inf} and low T_{inf} groups of T cells, respectively. The highest differentially expressed genes revealed clusters similar to previously described T cell phenotypes in breast cancer, including $CD4^+IL7R^+$, $CD4^+FOXP3^+$, resident memory $CD8^+$ T cells ($CD8^+$ Trm cells), and 1 population described in lung cancer and liver cancer with high granulysin expression, $CD4^+GNLY^+$ (Figures 4C–4F, S5, and S6) (Savas et al., 2018; Guo et al., 2018; Zheng et al., 2017a). $IFNG$ expressing $CD8^+$ Trm clusters were present in both groups. Both groups also had $CD4^+IL7R^+$ and $CD4^+FOXP3^+$ T cell clusters. The high T_{inf} group had an extra $CD4^+GNLY^+$ (adjusted $p = 6.09 \times 10^{-18}$) cluster. Contrastingly, $GNLY$ was expressed in the low T_{inf} group by $CD8^+$ Trm cluster (adjusted $p = 1.64 \times 10^{-6}$) (Figures 4D, 4F, and S6; Table S5). TOX was only significantly highly expressed (adjusted $p = 4.23 \times 10^{-3}$) by the $CD8^+$ Trm cluster in the high T_{inf} group, but not differentially expressed in the low T_{inf} group clusters (Figures 4C and 4D; Table S5). TOX^+ T cells persist during chronic infection, and TOX is expressed by the $CD8^+$ T cells

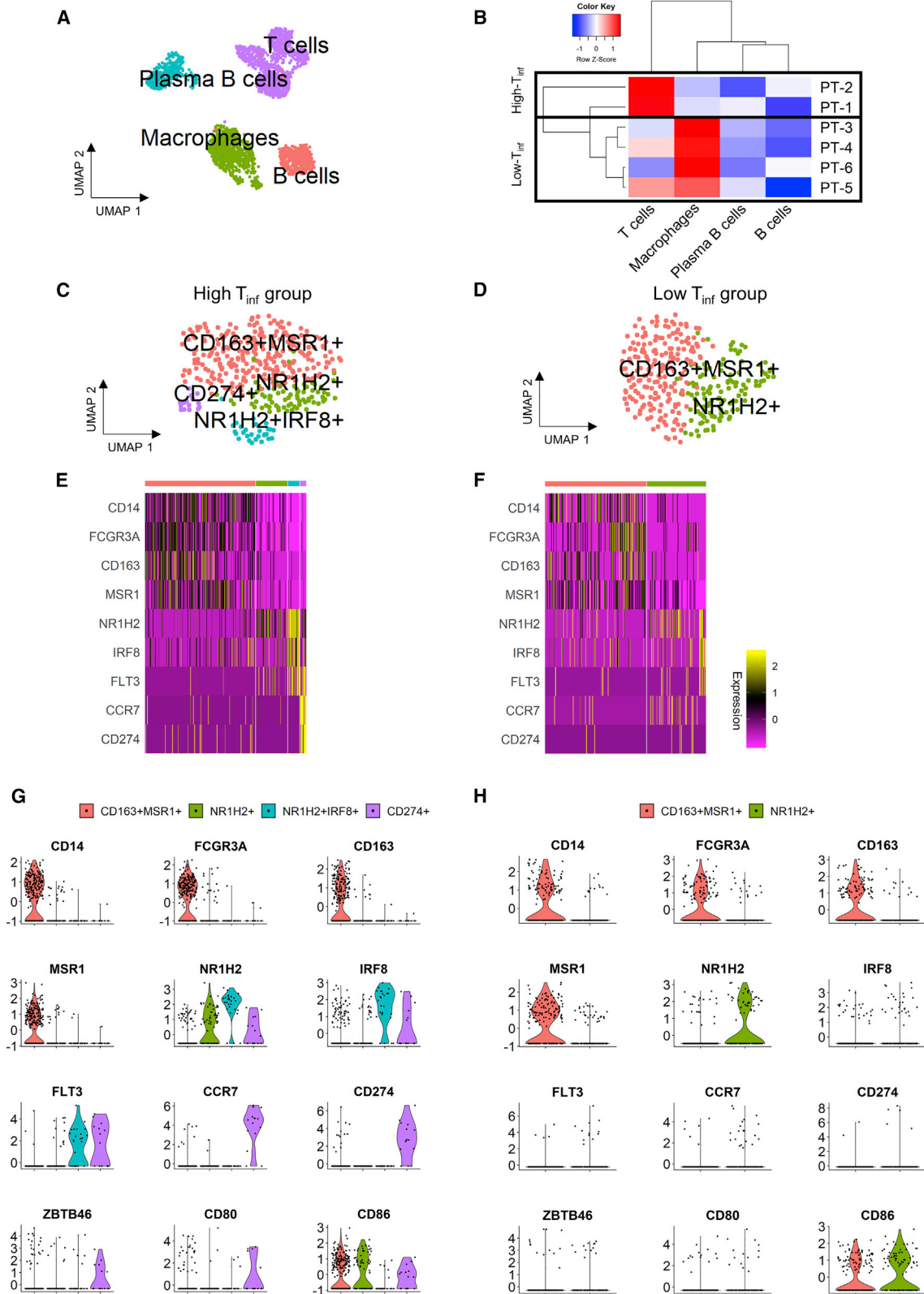
that are reactivated in response to programmed death-ligand 1 (PD-L1) immunotherapy (Yao et al., 2019; Khan et al., 2019). $CD8^+$ Trm cluster in the high T_{inf} group (Figure 4A) expressed TOX , $LAG3$, and $TIGIT$ (Figures 4E and 4F). The positive Pearson correlation between TOX and markers of exhaustion suggests that TOX^+ T are exhausted T cells (Table S5). Based on TCGA ovarian cancer data, the co-expression of $CD8$ and TOX was statistically significant in the immunoreactive subtype ($p = 6.123 \times 10^{-7***}$), the mesenchymal subtype ($p = 0.0018**$), and positive but not significant in the differentiated subtype ($p = 0.0603$). The correlation between $CD4$ and $GNLY$ was significant in the differentiated subtype ($p = 3.383 \times 10^{-5***}$), the mesenchymal subtype ($p = 0.0280^*$), the proliferative subtype ($p = 0.0013^*$), and positive but not significant in the immunoreactive subtype ($p = 0.0636$; Table S6). According to the Mayo Clinic ovarian cancer cohort, patients within the immunoreactive subtype followed by the differentiated subtype displayed the longest survival (Konecny et al., 2014). Our data provide insights into molecular markers that correlate and may be responsible for the increased overall survival displayed by patients in the immunoreactive subtype.

Transcriptionally distinct plasmablast and plasma cell cluster in high T_{inf} group

To investigate the B cell subtypes in our samples, both naive and plasma B cells were clustered yielding 4 and 2 clusters in high T_{inf} and low T_{inf} groups, respectively (Figures 5A and 5B). In the high T_{inf} and low T_{inf} groups, the naive cluster highly expressed major histocompatibility complex (MHC) class II genes ($HLA.DRA$, $HLA.DPA1$, $HLA.DQA1$) (Figures 5C, 5D, and S5; Table S7). Tumor-associated B cell subpopulations have previously been defined; we assessed our dataset for these subsets using a combination of gene expression and Pearson correlation (Griss et al., 2019). In the high T_{inf} group, there were 3 $PRDM1^+$ clusters: $SDC1^+$ plasma cells, $CD38^+$ germinal center B cells, and the final cluster highly expressed MHC class II genes, as well as $MKI67$ (adjusted $p = 2.16 \times 10^{-6}$), suggesting a plasmablast population (Figures 5C, 5D, and S5; Table S7). Pearson correlation was used to confirm co-expression between $PRDM1$ and other marker genes in each B cell subset (Table S7). The $PRDM1^+$ cluster in the low T_{inf} group expressed $CD38$, suggesting that they are germinal center B cells. The presence of tertiary lymphoid structures was confirmed using H&E and CD19 IHC staining (Figure S7). Activated B cells produce $IFNG$, so we assessed our data for $IFNG$ expression in the B cell subsets (Olekan et al., 2015). Plasmablasts expressed $IFNG$ in the high T_{inf} group, while none of the B cell clusters in the low T_{inf} group expressed $IFNG$ (Figure S5). Together with the T cell data, these results suggest that B cells may contribute to the immune response within the tumor microenvironment.

Figure 2. Cell-type and molecular subtype assignment using Drop-seq data

- UMAP of high-quality cells from all 6 metastatic ovarian cancer samples from the omentum, colored by clustering results.
- Ratio of cellular composition in each patient sample.
- Cancer subtype designation for each patient sample based on TCGA classification.
- Cancer subtype designation by cell type based on TCGA.
- UMAP and heatmap of top 10 genes per subcluster derived from epithelial cells and ESCs.
- Feature plots of relevant marker genes of 4,733 cells in the epithelial cell cluster, aggregated from all samples.



(legend on next page)

DISCUSSION

The transcriptomic data of the 9,885 cells (not including adipocytes; see [Method details](#)) collected from omental tumor samples in this study provide a holistic insight into the tumor microenvironment of metastatic ovarian cancer. Mapping our cells to curated cell types from the CellAtlas along with Gene Ontology and pathway-based enrichment allowed robust cell-type assignment compared to cell markers alone. Our approach allowed us to simultaneously analyze the cancer and stromal compartments of the tumor microenvironment with an emphasis on the different immune cell types and subsets. We identified unique subpopulations such as CD274⁺ and IRF8⁺ macrophages, CD4⁺GNLY⁺ T cells, plasmablasts, and plasma B cells. This comprehensive approach helps unravel the interactions between the cells within metastatic ovarian tumors at single-cell resolution.

The largest cluster of cells was cancer epithelial cells, which composed ~50% of the cells analyzed. Cells of the epithelial subclusters expressed various genes associated with metastatic disease, including *MUC16* and *PAX8*, while other subclusters highly expressed EMT marker, vimentin. Of particular interest was the presence of cancer stem cells (CSCs), a potentially useful therapeutic approach to target ovarian cancer ([Bast et al., 2009](#)). Like previous studies, we were unable to identify cells that co-expressed known markers of stem cells ([Shah and Landen, 2014](#); [Burgos-Ojeda et al., 2012](#)). However, we identified a cell population closely resembling ESCs and adjacent to the epithelial cell cluster that highly expressed proliferative marker, *MKI67*. Successful identification, isolation, and interrogation of putative ESCs may provide useful insights about CSCs in ovarian cancer.

Our data revealed a positive correlation between the presence of adipocytes (by IHC) and immune cells (by Drop-seq). However, infiltration of immune cells into the omentum during metastatic cancer does not always elicit anti-tumor responses ([Oosterling et al., 2006](#)). To this end, we sought to transcriptionally characterize the immune cells within our samples. Our patient samples stratified into 2 groups: high T_{inf} and low T_{inf}, based on similar T cell populations. In addition, our data revealed transcriptionally distinct subclusters unique to macrophage and B cell clusters in the high T_{inf} group. For macrophages, in addition to the 2 clusters present in both groups, there were 2 clusters, NR1H2⁺IRF8⁺ and CD274⁺ clusters, present only in the high T_{inf} group. *IRF8* and *CD274* are upregulated in an activation-dependent manner, suggesting that the high T_{inf} group may be mounting an anti-tumor immune response. NR1H2⁺IRF8⁺ and CD274⁺ clusters share similar gene expression, closely resembling M1 macrophages. It could be that the macrophages in the NR1H2⁺IRF8⁺ cluster are in a transitional state; therefore, stimulating them to becoming M1 macrophages may be another approach for cancer immunotherapy.

T cells are the central players in most immunotherapeutic approaches in oncology ([Sharma and Allison, 2015](#)). In our study, we identified *GNLY* expressing CD4⁺ T cells and *TOX* expressing CD8⁺ Trm cells in our high T_{inf} group. Previous T cell profiling studies have identified CD4⁺GNLY⁺ T cells in lung and liver cancer ([Zheng et al., 2017a](#); [Guo et al., 2018](#)). These cells are suggested to have cytotoxic function similar to cytotoxic CD8⁺ T cells and may provide a viable approach to cancer therapy. Advances in personalized medicine have revealed *TOX* as a transcription factor expressed by T cells that respond to immune checkpoint blockade ([Yao et al., 2019](#); [Siddiqui et al., 2019](#)). In our tumor samples, *TOX* was mainly expressed by the CD8⁺ Trm cluster in the high T_{inf} group. *IFNG* from cells of the CD8⁺ Trm cluster in the high T_{inf} may be responsible for the induction of *IRF8* in macrophages. Interestingly, *GNLY* was expressed by the CD4⁺GNLY⁺ cluster in the high T_{inf} group and CD8⁺ Trm cluster in the low T_{inf} group. The differences in the effect of granulysin from CD4⁺ T cells and CD8⁺ T cells on cancer cells need to be investigated. Tumors can be categorized based on their immunoscore (the basal immune response within the tumor) from cold tumors to hot tumors to help guide the personalization of cancer therapy ([Galon and Bruni, 2019](#)). Future scRNA-seq analysis of T cells sampled from different regions of tumors of different immunoscores will be informative in guiding immunotherapeutic approaches. Our scRNA-seq data (high T_{inf} group), bulk RNA-seq from TCGA and Mayo Clinic data (immunoreactive and differentiated molecular subtypes), taken together reveal that a high infiltration of CD8⁺TOX⁺ and CD4⁺GNLY⁺ T cells may be a good indicator of patient survival in ovarian cancer.

Tertiary lymphoid structures were detected in almost all tumor samples, albeit to varying extents. The high T_{inf} and low T_{inf} groups had germinal center B cells (PRDMI⁺CD38⁺). Interestingly, the high T_{inf} group also had unique B cell subsets, including (PRDMI⁺SDC1⁺) plasma cells and *IFNG* expressing plasmablasts (PRDMI⁺CD38⁺MKI67⁺). Previous study of tumor-induced plasmablast-like B cell population supports the presence of these cells in patients who respond to immune checkpoint blockade ([Griss et al., 2019](#)). In addition, these plasmablast-like cells increase PD-1⁺ T cell activation ([Griss et al., 2019](#)). It will be useful to investigate the role of antigen-cognate plasmablasts in the generation and/or maintenance of *TOX*⁺ T cells. Furthermore, these plasmablast-like cells expressed macrophage chemo-attractants and correlated positively with the presence of CD8a ([Griss et al., 2019](#)). These studies, combined with our current data, suggest an association between plasmablast-like B cells, CD8⁺TOX⁺ and CD4⁺GNLY⁺ T cells, and NR1H2⁺IRF8⁺ and CD274⁺ macrophages. A mechanistic study of these plasmablast-like and plasma B cells within the tumor microenvironment is necessary to improve patient's response to immune checkpoint inhibitors.

Figure 3. scRNA-seq data of annotated immune population from all 6 patient samples

(A) UMAP of immune cells showing the 4 main immune cell types based on correlation with CellAtlas cell type.
 (B) Heatmap of immune cell types (T cell, B cell, plasma B cell, and macrophage) in each patient sample with dendrograms on cell types (columns) and patients (rows), dividing the samples into high and low T cell infiltration (T_{inf}) groups.
 (C and D) UMAP plots of unsupervised clustering of annotated macrophages from (C) high T_{inf} (383 cells) and (D) low T_{inf} (312 cells) groups.
 (E and F) Heatmaps from immune cells showing differentially expressed markers between clusters in (E) high T_{inf} and (F) low T_{inf} groups.
 (G and H) Feature plots of expression in relevant genes in macrophages in high and low T_{inf} groups, respectively.

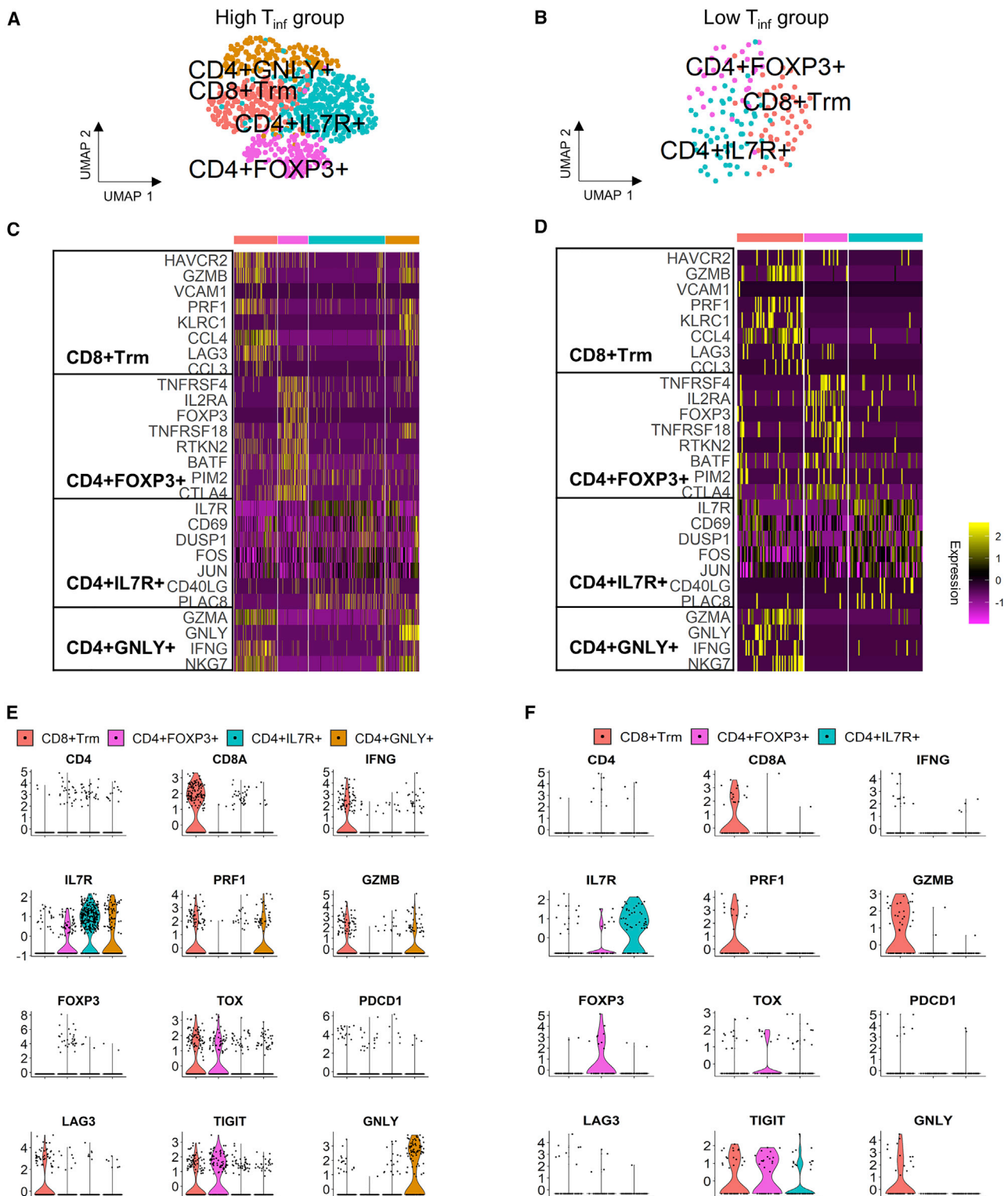


Figure 4. Characterization of annotated T cell population

(A and B) UMAP of T cells in (A) high T_{inf} (820 cells) and (B) low T_{inf} (136 cells) groups.

(C and D) Heatmaps of key genes in different clusters in (C) high T_{inf} and (D) low T_{inf} groups. Clusters in heatmaps are indicated by the same color as in the UMAP plots.

(E and F) Violin plots showing scaled log-normalized expression values of key genes in (E) high T_{inf} and (F) low T_{inf} groups.

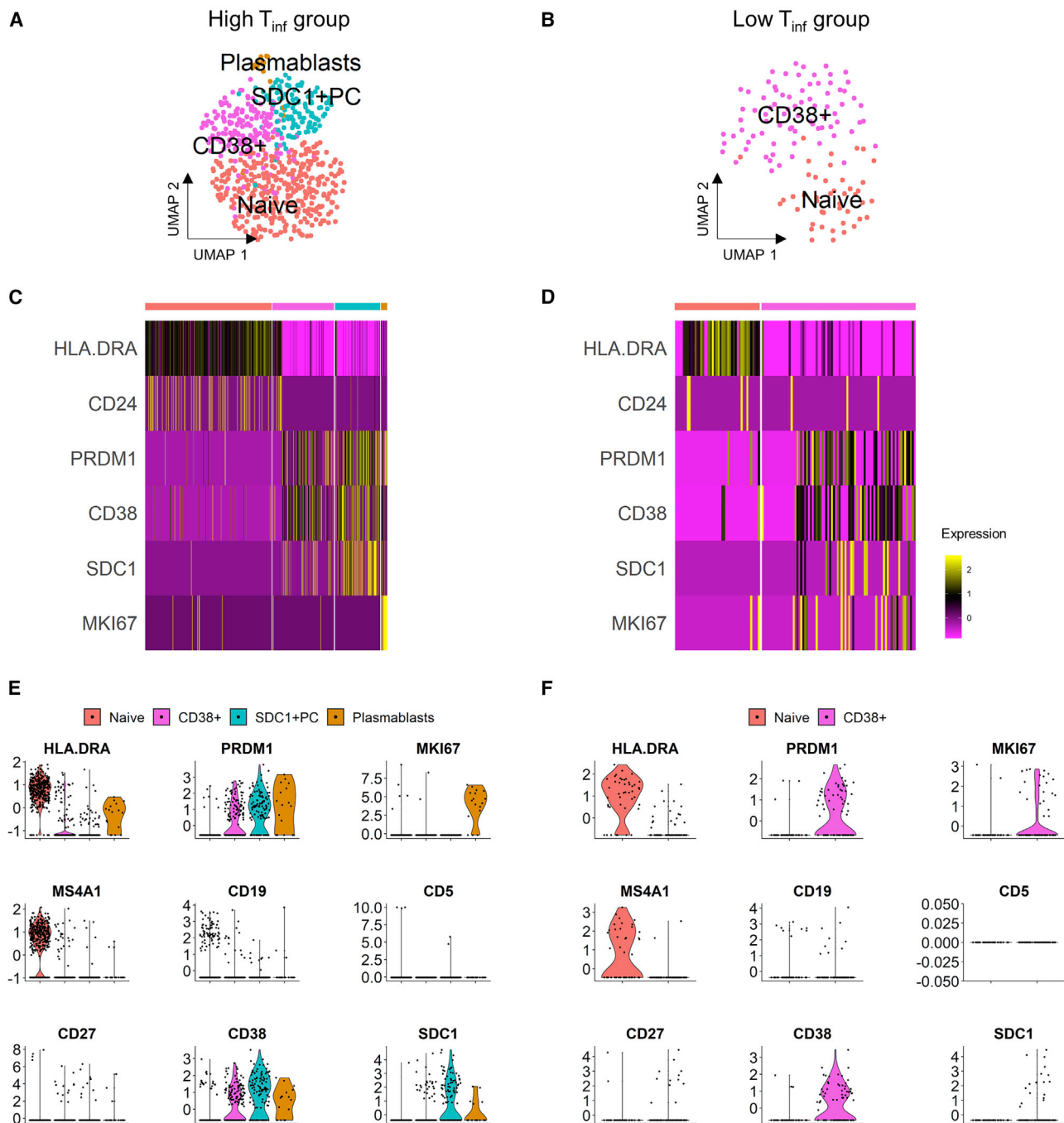


Figure 5. Identification of B cell clusters across all patient samples

(A and B) UMAP plot for B cells in (A) high T_{inf} (396 cells) and (B) low T_{inf} (124 cells) groups.

(C and D) Heatmaps of key genes in different clusters in (C) high T_{inf} and (D) low T_{inf} groups. Clusters in heatmap are indicated by the same color as in the UMAPs.

(E and F) Violin plots showing scaled log-normalized expression values of key genes in (E) high T_{inf} and (F) low T_{inf} groups.

In addition to the major cell types analyzed, there were other clusters, including 1 each of endothelial cell, mesenchymal stem cell, and fibroblast, and 3 clusters of undecided cell types (N1, N2, N3). Endothelial cells line the luminal side of blood vessels and are necessary for the metastasis of ovarian cancer cells (Hanahan and Folkman, 1996). Fibroblast growth factor 18

(*FGF18*) expressed by the cancer epithelial cells in our dataset may enhance tumor angiogenesis (Figure S7) (Wei et al., 2013). The MSCs were transcriptionally closest to the fibroblasts. Inflamed omentum contains stem cells displaying similar surface markers to MSCs (Shah et al., 2012; Friedenstein et al., 1968). These stem cells are capable of differentiating into fat, cartilage,

or bone, depending on the secreted factors present (Shah et al., 2012; Friedenstein et al., 1968). Finally, there was a distinct fibroblast cluster in our samples. Metastatic transformation of the omentum changes the cellular composition from mainly adipocytes to cancer cells, immune cells, and fibroblasts (Pearce et al., 2018). Cancer-associated fibroblasts (CAFs) mainly function to remodel the extracellular matrix in the tumor microenvironment (Kalluri, 2016). Recently, a scRNA-seq study of CAFs in pancreatic cancer revealed a *LRRC15*⁺ CAF population that correlated with poor response in patients treated with anti-PD-L1 therapy (Dominguez et al., 2020). We identified *LRRC15* expressing fibroblasts in our dataset (Figure S7). However, their function in ovarian cancer immunotherapy needs to be investigated.

The undecided clusters, from mapping to the CellAtlas cell types, best correlate with astrocytes (N1), common myeloid progenitor (CMP)/bone marrow progenitor (N2), and plasmacytoid dendritic cells (N3), respectively. Although we were interested in the dendritic cell population, we were restricted from further analysis due to low cell count (<60). We also note that adipocytes were separated during centrifugation after tumor digestion and not included in the single-cell experiments. While a previous scRNA-seq study reported the presence of mesothelial cells in benign ovarian tumors (Shih et al., 2018), we did not detect mesothelial cells in our metastatic dataset from the omentum.

Limitations of study

We note that our study was limited by the small number of patients and mix of histotypes. Our plan to include more HGSOC or non-HGSOC samples was hindered by the current coronavirus disease 2019 (COVID-19) pandemic, which resulted in the cancellation of surgeries, difficulty in consenting patients, and limited availability of fresh samples. To ensure that the sample of MMMT histotype was not unduly influencing our conclusions, we repeated our analyses after excluding the MMMT sample and validated our results on HGSOC and serous samples.

This scRNA-seq study allows the stratification of patient solid tumor samples initially pathologically classified as stage III or greater, based on immune cellular composition of metastatic ovarian cancer. Concurrent transcriptomic analysis of cancer and stromal cells revealed patient heterogeneity, highlighting the need for personalized medicine. Interrogating tumor-infiltrating lymphocytes at the single-cell level also revealed tumor-intrinsic responses in ovarian cancer. Ultimately, follow-up mechanistic studies are required to further elucidate the roles of the transcriptionally distinct immune cell clusters and how they can be manipulated to enhance immunotherapeutic approaches.

STAR★METHODS

Detailed methods are provided in the online version of this paper and include the following:

- KEY RESOURCES TABLE
- RESOURCE AVAILABILITY
 - Lead contact
 - Materials availability
 - Data and code availability

- EXPERIMENTAL MODEL AND SUBJECT DETAILS
- METHOD DETAILS
 - Immunohistochemistry
 - Tissue digestion, red blood cell lysis and dead cell removal
 - Drop-seq experiments
 - Data processing, alignment and clustering analysis
 - Cancer subtype classification and correlation with The Cancer Genome Atlas
 - Cell type classification and correlation with CellAtlas
 - Classification with cluster markers, canonical genes, and genetic functions
 - Marker identification for subtypes of various cell populations
 - Comparison and validation with bulk sequencing data from The Cancer Genome Atlas (TCGA) program
- QUANTIFICATION AND STATISTICAL ANALYSIS

SUPPLEMENTAL INFORMATION

Supplemental information can be found online at <https://doi.org/10.1016/j.celrep.2021.109165>.

ACKNOWLEDGMENTS

We are grateful to Drs. Mengjie Chen, Marcus Clark, and Ernst Lengyel for helpful discussions and Dr. Mark Lingen for tissue access. All of the tissues were histologically graded, de-identified, and obtained from the University of Chicago Human Tissue Resource Center. Computational resources and data storage were provided by the University of Chicago Research Computing Center. This work was internally funded.

AUTHOR CONTRIBUTIONS

S.O. and A.B. conceived and designed the study. S.O. performed all single-cell dissociation and scRNA-seq experiments, with support from R.B. and H.E. B.X. conducted all of the scRNA-seq data analysis, and S.O. and A.B. interpreted the data. S.O. and B.X. wrote the manuscript, with oversight by A.B.

DECLARATION OF INTERESTS

A.B. is a consultant for Novartis Institutes for BioMedical Research. All of the other authors declare no competing interests.

INCLUSION AND DIVERSITY

One or more of the authors of this paper self-identifies as an underrepresented ethnic minority in science. The author list of this paper includes contributors from the location where the research was conducted who participated in the data collection, design, analysis, and/or interpretation of the work.

Received: July 11, 2020
Revised: January 4, 2021
Accepted: May 3, 2021
Published: May 25, 2021

REFERENCES

- A-González, N., and Castrillo, A. (2011). Liver X receptors as regulators of macrophage inflammatory and metabolic pathways. *Biochim. Biophys. Acta* 1812, 982–994.
- Bast, R.C., Jr., Hennessy, B., and Mills, G.B. (2009). The biology of ovarian cancer: new opportunities for translation. *Nat. Rev. Cancer* 9, 415–428.

- Burgos-Ojeda, D., Rueda, B.R., and Buckanovich, R.J. (2012). Ovarian cancer stem cell markers: prognostic and therapeutic implications. *Cancer Lett.* **322**, 1–7.
- Butler, A., Hoffman, P., Smibert, P., Papalexi, E., and Satija, R. (2018). Integrating single-cell transcriptomic data across different conditions, technologies, and species. *Nat. Biotechnol.* **36**, 411–420.
- Castrillo, A., Joseph, S.B., Marathe, C., Mangelsdorf, D.J., and Tontonoz, P. (2003). Liver X receptor-dependent repression of matrix metalloproteinase-9 expression in macrophages. *J. Biol. Chem.* **278**, 10443–10449.
- Chen, J., Bardes, E.E., Aronow, B.J., and Jegga, A.G. (2009). ToppGene Suite for gene list enrichment analysis and candidate gene prioritization. *Nucleic Acids Res.* **37**, W305–W311.
- Chen, M., Zhan, Q., Mu, Z., Wang, L., Zheng, Z., Miao, J., Zhu, P., and Li, Y.I. (2021). Alignment of single-cell RNA-seq samples without overcorrection using kernel density matching. *Genome Res.* **31**, 698–712.
- Clark, R., Krishnan, V., Schoof, M., Rodriguez, I., Theriault, B., Chekmareva, M., and Rinker-Schaeffer, C. (2013). Milky spots promote ovarian cancer metastatic colonization of peritoneal adipose in experimental models. *Am. J. Pathol.* **183**, 576–591.
- Dixit, A., Parnas, O., Li, B., Chen, J., Fulco, C.P., Jerby-Aron, L., Marjanovic, N.D., Dionne, D., Burks, T., Raychowdhury, R., et al. (2016). Perturb-Seq: Dissecting Molecular Circuits with Scalable Single-Cell RNA Profiling of Pooled Genetic Screens. *Cell* **167**, 1853–1866.e17.
- Dobin, A., Davis, C.A., Schlesinger, F., Drenkow, J., Zaleski, C., Jha, S., Batut, P., Chaisson, M., and Gingeras, T.R. (2013). STAR: ultrafast universal RNA-seq aligner. *Bioinformatics* **29**, 15–21.
- Dominguez, C.X., Müller, S., Keerthivasan, S., Koeppen, H., Hung, J., Gierke, S., Breart, B., Foreman, O., Bainbridge, T.W., Castiglioni, A., et al. (2020). Single-Cell RNA Sequencing Reveals Stromal Evolution into LRRC15⁺ Myofibroblasts as a Determinant of Patient Response to Cancer Immunotherapy. *Cancer Discov.* **10**, 232–253.
- Frankish, A., Diekhans, M., Ferreira, A.M., Johnson, R., Jungreis, I., Loveland, J., Mudge, J.M., Sisu, C., Wright, J., Armstrong, J., et al. (2019). GENCODE reference annotation for the human and mouse genomes. *Nucleic Acids Res.* **47** (D1), D766–D773.
- Friedenstein, A.J., Petrakova, K.V., Kurolesova, A.I., and Frolova, G.P. (1968). Heterotopic of bone marrow. Analysis of precursor cells for osteogenic and hematopoietic tissues. *Transplantation* **6**, 230–247.
- Galon, J., and Bruni, D. (2019). Approaches to treat immune hot, altered and cold tumours with combination immunotherapies. *Nat. Rev. Drug Discov.* **18**, 197–218.
- Griss, J., Bauer, W., Wagner, C., Simon, M., Chen, M., Grabmeier-Pfistershammer, K., Maurer-Granofsky, M., Roka, F., Penz, T., Bock, C., et al. (2019). B cells sustain inflammation and predict response to immune checkpoint blockade in human melanoma. *Nat. Commun.* **10**, 4186.
- Guo, X., Zhang, Y., Zheng, L., Zheng, C., Song, J., Zhang, Q., Kang, B., Liu, Z., Jin, L., Xing, R., et al. (2018). Publisher correction: global characterization of T cells in non-small-cell lung cancer by single-cell sequencing. *Nat. Med.* **24**, 1628.
- Gupta, M., Shin, D.M., Ramakrishna, L., Goussetis, D.J., Platanius, L.C., Xiong, H., Morse, H.C., 3rd, and Ozato, K. (2015). IRF8 directs stress-induced autophagy in macrophages and promotes clearance of *Listeria monocytogenes*. *Nat. Commun.* **6**, 6379.
- Hanahan, D., and Folkman, J. (1996). Patterns and emerging mechanisms of the angiogenic switch during tumorigenesis. *Cell* **86**, 353–364.
- Hu, Z., Artibani, M., Alsaadi, A., Wietek, N., Morotti, M., Shi, T., Zhong, Z., Santana Gonzalez, L., El-Sahhar, S., KaramiNejadRanjbar, M., et al. (2020). The Repertoire of Serous Ovarian Cancer Non-genetic Heterogeneity Revealed by Single-Cell Sequencing of Normal Fallopian Tube Epithelial Cells. *Cancer Cell* **37**, 226–242.e7.
- Hylland, B., Repasky, E., Shrikant, P., Intengan, M., Beck, A., Driscoll, D., Singhal, P., Lele, S., and Odunsi, K. (2006). Expression of Wilms tumor gene (WT1) in epithelial ovarian cancer. *Gynecol. Oncol.* **101**, 12–17.
- Izar, B., Tirosh, I., Stover, E.H., Wakiro, I., Cuoco, M.S., Alter, I., Rodman, C., Leeson, R., Su, M.J., Shah, P., et al. (2020). A single-cell landscape of high-grade serous ovarian cancer. *Nat. Med.* **26**, 1271–1279.
- Jaitin, D.A., Weiner, A., Yofe, I., Lara-Astiaso, D., Keren-Shaul, H., David, E., Salame, T.M., Tanay, A., van Oudenaarden, A., and Amit, I. (2016). Dissecting Immune Circuits by Linking CRISPR-Pooled Screens with Single-Cell RNA-Seq. *Cell* **167**, 1883–1896.e15.
- Kalluri, R. (2016). The biology and function of fibroblasts in cancer. *Nat. Rev. Cancer* **16**, 582–598.
- Khan, O., Giles, J.R., McDonald, S., Manne, S., Ngiew, S.F., Patel, K.P., Werner, M.T., Huang, A.C., Alexander, K.A., Wu, J.E., et al. (2019). TOX transcriptionally and epigenetically programs CD8⁺ T cell exhaustion. *Nature* **571**, 211–218.
- Klemba, A., Purzycka-Olewiecka, J.K., Wcislo, G., Czarnecka, A.M., Lewicki, S., Lesyng, B., Szczylik, C., and Kieda, C. (2018). Surface markers of cancer stem-like cells of ovarian cancer and their clinical relevance. *Contemp. Oncol. (Pozn.)* **22** (1A), 48–55.
- Konecny, G.E., Wang, C., Hamidi, H., Winterhoff, B., Kalli, K.R., Dering, J., Ginther, C., Chen, H.W., Dowdy, S., Cliby, W., et al. (2014). Prognostic and therapeutic subtypes of molecular subtypes in high-grade serous ovarian cancer. *J. Natl. Cancer Inst.* **106**, dju249.
- Krist, L.F., Kerremans, M., Broekhuis-Fluitsma, D.M., Eestermans, I.L., Meyer, S., and Beelen, R.H. (1998). Milky spots in the greater omentum are predominant sites of local tumour cell proliferation and accumulation in the peritoneal cavity. *Cancer Immunol. Immunother.* **47**, 205–212.
- Kristiansen, G., Denkert, C., Schlüns, K., Dahl, E., Pilarsky, C., and Hauptmann, S. (2002). CD24 is expressed in ovarian cancer and is a new independent prognostic marker of patient survival. *Am. J. Pathol.* **161**, 1215–1221.
- Ma, J., Liu, L., Che, G., Yu, N., Dai, F., and You, Z. (2010). The M1 form of tumor-associated macrophages in non-small cell lung cancer is positively associated with survival time. *BMC Cancer* **10**, 112.
- Mabbott, N.A., Baillie, J.K., Brown, H., Freeman, T.C., and Hume, D.A. (2013). An expression atlas of human primary cells: inference of gene function from coexpression networks. *BMC Genomics* **14**, 632.
- Macosko, E.Z., Basu, A., Satija, R., Nemes, J., Shekhar, K., Goldman, M., Tirosh, I., Bialas, A.R., Kamitaki, N., Martersteck, E.M., et al. (2015). Highly Parallel Genome-wide Expression Profiling of Individual Cells Using Nanoliter Droplets. *Cell* **161**, 1202–1214.
- McInnes, L., Healy, J., and Melville, J. (2018). UMAP: Uniform Manifold Approximation and Projection for Dimension Reduction. *J. Open Source Softw.* **29**, 861.
- Nieman, K.M., Kenny, H.A., Penicka, C.V., Ladanyi, A., Buell-Gutbrod, R., Zillhardt, M.R., Romero, I.L., Carey, M.S., Mills, G.B., Hotamisligil, G.S., et al. (2011). Adipocytes promote ovarian cancer metastasis and provide energy for rapid tumor growth. *Nat. Med.* **17**, 1498–1503.
- Olalekan, S.A., Cao, Y., Hamel, K.M., and Finnegan, A. (2015). B cells expressing IFN- γ suppress Treg-cell differentiation and promote autoimmune experimental arthritis. *Eur. J. Immunol.* **45**, 988–998.
- Oosterling, S.J., van der Bij, G.J., Bögels, M., van der Sijp, J.R., Beelen, R.H., Meijer, S., and van Egmond, M. (2006). Insufficient ability of omental milky spots to prevent peritoneal tumor outgrowth supports omentectomy in minimal residual disease. *Cancer Immunol. Immunother.* **55**, 1043–1051.
- Pearce, O.M.T., Delaine-Smith, R.M., Maniati, E., Nichols, S., Wang, J., Böhm, S., Rajeeve, V., Ullah, D., Chakravarty, P., Jones, R.R., et al. (2018). Deconstruction of a Metastatic Tumor Microenvironment Reveals a Common Matrix Response in Human Cancers. *Cancer Discov.* **8**, 304–319.
- Platell, C., Cooper, D., Papadimitriou, J.M., and Hall, J.C. (2000). The omentum. *World J. Gastroenterol.* **6**, 169–176.
- Robertson, D.M., Cahir, N., Burger, H.G., Marners, P., McCloud, P.I., Pettersson, K., and McGuckin, M. (1999). Combined inhibin and CA125 assays in the detection of ovarian cancer. *Clin. Chem.* **45**, 651–658.
- Santoiemma, P.P., and Powell, D.J., Jr. (2015). Tumor infiltrating lymphocytes in ovarian cancer. *Cancer Biol. Ther.* **16**, 807–820.

- Savas, P., Virassamy, B., Ye, C., Salim, A., Mintoff, C.P., Caramia, F., Salgado, R., Byrne, D.J., Teo, Z.L., Dushyanthen, S., et al. (2018). Single-cell profiling of breast cancer T cells reveals a tissue-resident memory subset associated with improved prognosis. *Nat. Med.* **24**, 986–993.
- Schwede, M., Waldron, L., Mok, S.C., Wei, W., Basunia, A., Merritt, M.A., Mitsiades, C.S., Parmigiani, G., Harrington, D.P., Quackenbush, J., et al. (2020). The Impact of Stroma Admixture on Molecular Subtypes and Prognostic Gene Signatures in Serous Ovarian Cancer. *Cancer Epidemiol. Biomarkers Prev.* **29**, 509–519.
- Selewa, A., Dohn, R., Eckart, H., Lozano, S., Xie, B., Gauchat, E., Elorbany, R., Rhodes, K., Burnett, J., Gilad, Y., et al. (2019). Systematic Comparison of High-throughput Single-Cell and Single-Nucleus Transcriptomes during Cardiomyocyte Differentiation. *Sci. Rep.* **10**, 1535.
- Servet-Delprat, C., Arnaud, S., Jurdic, P., Nataf, S., Grasset, M.F., Soulas, C., Domenget, C., Destaing, O., Rivollier, A., Perret, M., et al. (2002). *Fit3+* macrophage precursors commit sequentially to osteoclasts, dendritic cells and microglia. *BMC Immunol.* **3**, 15.
- Shah, M.M., and Landen, C.N. (2014). Ovarian cancer stem cells: are they real and why are they important? *Gynecol. Oncol.* **132**, 483–489.
- Shah, S., Lowery, E., Braun, R.K., Martin, A., Huang, N., Medina, M., Sethupathi, P., Seki, Y., Takami, M., Byrne, K., et al. (2012). Cellular basis of tissue regeneration by omentum. *PLoS ONE* **7**, e38368.
- Shalek, A.K., Satija, R., Adiconis, X., Gertner, R.S., Gaublomme, J.T., Raychowdhury, R., Schwartz, S., Yosef, N., Malboeuf, C., Lu, D., et al. (2013). Single-cell transcriptomics reveals bimodality in expression and splicing in immune cells. *Nature* **498**, 236–240.
- Sharma, P., and Allison, J.P. (2015). Immune checkpoint targeting in cancer therapy: toward combination strategies with curative potential. *Cell* **161**, 205–214.
- Shih, A.J., Menzin, A., Whyte, J., Lovecchio, J., Liew, A., Khalili, H., Bhuiya, T., Gregersen, P.K., and Lee, A.T. (2018). Correction: identification of grade and origin specific cell populations in serous epithelial ovarian cancer by single cell RNA-seq. *PLoS ONE* **13**, e0208778.
- Shimotsuma, M., Simpson-Morgan, M.W., Takahashi, T., and Hagiwara, A. (1992). Activation of omental milky spots and milky spot macrophages by intraperitoneal administration of a streptococcal preparation, OK-432. *Cancer Res.* **52**, 5400–5402.
- Siddiqui, I., Schaeuble, K., Chennupati, V., Fuertes Marraco, S.A., Calderon-Copete, S., Pais Ferreira, D., Carmona, S.J., Scarpellino, L., Gfeller, D., Pradervand, S., et al. (2019). Intratumoral Tcf1⁺PD-1⁺CD8⁺ T Cells with Stem-like Properties Promote Tumor Control in Response to Vaccination and Checkpoint Blockade Immunotherapy. *Immunity* **50**, 195–211.e10.
- Siegel, R.L., Miller, K.D., and Jemal, A. (2017). Cancer Statistics, 2017. *CA Cancer J. Clin.* **67**, 7–30.
- Stuart, T., Butler, A., Hoffman, P., Hafemeister, C., Papalexi, E., Mauck, W.M., 3rd, Hao, Y., Stoerckius, M., Smibert, P., and Satija, R. (2019). Comprehensive Integration of Single-Cell Data. *Cell* **177**, 1888–1902.e21.
- Testa, U., Castelli, G., and Pelosi, E. (2018). Genetic Abnormalities, Clonal Evolution, and Cancer Stem Cells of Brain Tumors. *Med. Sci. (Basel)* **6**, 85.
- The Cancer Genome Atlas Research Network (2011). Integrated genomic analyses of ovarian carcinoma. *Nature* **474**, 609–615.
- Thériault, C., Pinard, M., Comamala, M., Migneault, M., Beaudin, J., Matte, I., Boivin, M., Piché, A., and Rancourt, C. (2011). MUC16 (CA125) regulates epithelial ovarian cancer cell growth, tumorigenesis and metastasis. *Gynecol. Oncol.* **121**, 434–443.
- Tirosh, I., Izar, B., Prakadan, S.M., Wadsworth, M.H., 2nd, Treacy, D., Trombetta, J.J., Rotem, A., Rodman, C., Lian, C., Murphy, M., et al. (2016). Dissecting the multicellular ecosystem of metastatic melanoma by single-cell RNA-seq. *Science* **352**, 189–196.
- Tothill, R.W., Tinker, A.V., George, J., Brown, R., Fox, S.B., Lade, S., Johnson, D.S., Trivett, M.K., Etemadmoghadam, D., Locandro, B., et al.; Australian Ovarian Cancer Study Group (2008). Novel molecular subtypes of serous and endometrioid ovarian cancer linked to clinical outcome. *Clin. Cancer Res.* **14**, 5198–5208.
- Villani, A.C., Satija, R., Reynolds, G., Sarkizova, S., Shekhar, K., Fletcher, J., Griesbeck, M., Butler, A., Zheng, S., Lazo, S., et al. (2017). Single-cell RNA-seq reveals new types of human blood dendritic cells, monocytes, and progenitors. *Science* **356**, eaah4573.
- Waltman, L., and Eck, N.J.V. (2013). A smart local moving algorithm for large-scale modularity-based community detection. *Eur. Phys. J. B* **86**, 471.
- Wei, W., Mok, S.C., Oliva, E., Kim, S.H., Mohapatra, G., and Birrer, M.J. (2013). FGF18 as a prognostic and therapeutic biomarker in ovarian cancer. *J. Clin. Invest.* **123**, 4435–4448.
- Yao, C., Sun, H.W., Lacey, N.E., Ji, Y., Moseman, E.A., Shih, H.Y., Heuston, E.F., Kirby, M., Anderson, S., Cheng, J., et al. (2019). Single-cell RNA-seq reveals TOX as a key regulator of CD8⁺ T cell persistence in chronic infection. *Nat. Immunol.* **20**, 890–901.
- Yuan, A., Hsiao, Y.J., Chen, H.Y., Chen, H.W., Ho, C.C., Chen, Y.Y., Liu, Y.C., Hong, T.H., Yu, S.L., Chen, J.J., and Yang, P.C. (2015). Opposite Effects of M1 and M2 Macrophage Subtypes on Lung Cancer Progression. *Sci. Rep.* **5**, 14273.
- Zheng, C., Zheng, L., Yoo, J.K., Guo, H., Zhang, Y., Guo, X., Kang, B., Hu, R., Huang, J.Y., Zhang, Q., et al. (2017a). Landscape of Infiltrating T Cells in Liver Cancer Revealed by Single-Cell Sequencing. *Cell* **169**, 1342–1356.e16.
- Zheng, G.X., Terry, J.M., Belgrader, P., Ryvkin, P., Bent, Z.W., Wilson, R., Zirald, S.B., Wheeler, T.D., McDermott, G.P., Zhu, J., et al. (2017b). Massively parallel digital transcriptional profiling of single cells. *Nat. Commun.* **8**, 14049.

STAR★METHODS

KEY RESOURCES TABLE

REAGENT or RESOURCE	SOURCE	IDENTIFIER
Antibodies		
Anti-CD4	Abcam	Cat# Ab183685; RRID: AB_2686917
Anti-CD8a	Abcam	Cat# Ab237709
Anti-CD19	Abcam	Cat# Ab227688
Anti-Vimentin	Abcam	Cat# Ab16700; RRID:AB_443435
Anti-CD45	Agilent	Cat# M0701; RRID:AB_2314143
Anti-CD68	Abcam	Cat# Ab783; RRID: AB_306119
Anti-CD163	Abcam	Cat# Ab74604; RRID: AB_1280790
Anti-Cytokeratin-7	Thermo Scientific	Cat# MA5-11986; RRID:AB_10989596
Anti-TOX	ThermoFisher	Cat# PA5-53781; RRID:AB_2648830
Anti-GNLY	Abcam	Cat# Ab241511; RRID:AB_241511
Biological samples		
Human omental tissue	University of Chicago Human Tissue Resource Center	IRB18-0099
Chemicals, peptides, and recombinant proteins		
Penicillin-Streptomycin	GIBCO	Cat# 15140-122
Fetal Bovine Serum	ATCC	Cat# 302020
DMEM/F12- Dulbecco's Modified Eagle Medium	Thermo Fisher	Cat# 11330032
Phosphate Buffered Saline	Fisher bioreagents	Cat# BP399-500
Formaldehyde solution 4%, buffered pH 6.9	Sigma-Aldrich	Cat# 1004969010
Collagenase IV	Sigma-Aldrich	Cat# C5138
Hyaluronidase	Sigma-Aldrich	Cat# H3884-500MG
DNase I	GoldBio	Cat# D-301-100
HBSS Hank's balanced salt solution	Thermo Fisher	Cat# 14175-103
Bovine Serum Albumin (BSA) 20 mg/ml	New England Biolabs	Cat# B9000S
1M DTT Solution	Teknova	Cat# D9750
10% Sarkosyl Solution	Teknova	Cat# S3376
20% Ficoll Solution	Sigma	Cat# F5415-50ML
Ethylenediamine tetraacetate acid (EDTA) 0.5M, pH 8.0	Fisher	Cat# BP2482-500
Tris Hydrochloride 1M Solution, pH 7.5	Fisher bioreagents	Cat# BP1757-500
Droplet Generation Oil for EvaGreen	Bio-Rad	Cat# 1864006
20X SSC Molecular Biology Grade	Teknova	Cat# S0282
Tris-EDTA, 1X Solution pH 8.0	Fisher bioreagents	Cat# P2473-1
10% Tween-20 Solution	Teknova	Cat# T0710
10% SDS Solution	Teknova	Cat# S0288
Betaine Monohydrate	Sigma-Aldrich	Cat# 14300-500G
Magnesium Chloride Solution	Sigma-Aldrich	Cat# M1028-100ML
UltraPure PCR Deoxynucleotide Mix	Takara Bio	Cat# 639125
NxGen RNase Inhibitor	Lucigen	Cat# F83923
Maxima H Minus Reverse Transcriptase (200U/uL)	Fisher Scientific	Cat# EP0751
Exonuclease 1 (20U/uL)	New England BioLabs	Cat# M0293L
Kapa HiFi HotStart ReadyMix	Fisher	Cat# NC0465187
Absolute ethanol (200 Proof)	Fisher	Cat# BP2818-500
SPRI Select	Beckman Coulter	Cat# B23318

(Continued on next page)

Continued		
REAGENT or RESOURCE	SOURCE	IDENTIFIER
UltraPure Distilled Water	Invitrogen	Cat# 10977-015
Perfluorooctanol	Synquest Laboratories	Cat# 2101-3-29
PhiX Control V3	Illumina	Cat# FC-110-3001
Critical commercial assays		
Agilent high sensitivity chip	Agilent	Cat# 5067-4626
Nextera XT DNA kit	Illumina	Cat# FC-131-1096
Qubit dsDNA HS Assay kit	Thermo Scientific	Cat# Q32854
Dead cell removal kit	Miltenyi Biotec	Cat# 130-090-101
Red blood cell lysis kit	Miltenyi Biotec	Cat# 130-094-183
Deposited data		
Raw fastq and the processed digital gene expression matrix files	Gene Expression Omnibus	https://www.ncbi.nlm.nih.gov/geo/query/acc.cgi?acc=GSE147082
Oligonucleotides		
Barcoded beads	Chemgenes # CSO-2011	Bead-Linker -TTTTTTTAAAGCAG TGGTATCAACGCAGAGTACJJJ JJJJJJJJNNNNNNNNNTTTTTT TTTTTTTTTTTTTTTTTTTTTTTT
Template_Switch_Oligo	IDT, HPLC	AAGCAGTGGTATCAACG CAGAGTGAATrGrGrG
TSO_PCR	IDT, standard desalting	AAGCAGTGGTATCAACGCAGAGT
P5_TSO_Hybrid	IDT, HPLC	AATGATACGGCGACCA CCGAGATCTACACGCCTGTCC GCGGAAGCAGTGGTAT CAACGCAGAGT*A*C
Nextera_N701	IDT, standard desalting	CAAGCAGAAGACGGCAT ACGAGATTGCCTTAGT CTCGTGGGCTCGG
Read 1 Custom Primer	IDT, standard desalting	GCCTGTCCGCGGAAGCA GTGGTATCAACGCAGAGTAC
Software and algorithms		
GraphPad PRISM	https://www.graphpad.com/	Version 8.4.3
Aperio Imagescope	https://www.leicabiosystems.com	NA
Seurat	https://satijalab.org/seurat/	Version 3.1.4
R	https://www.r-project.org/	Version 3.6.1
dmatch	https://qzhan321.github.io/dmatch/	Version 0.1.8

RESOURCE AVAILABILITY

Lead contact

Further information and requests for resources and reagents should be directed to and will be fulfilled by the lead contact, Anindita Basu (onibasus@uchicago.com)

Materials availability

This study did not generate new unique reagents.

Data and code availability

The single cell dataset generated during this study have been deposited to Gene Expression Omnibus (GEO) repository (<https://www.ncbi.nlm.nih.gov/geo/>) with the dataset identifiers GSE147082.

EXPERIMENTAL MODEL AND SUBJECT DETAILS

Ovarian cancer tissue was collected from women undergoing debulking surgery at the University of Chicago Medical Center. Human tissue acquisition after patient deidentification was approved by the University of Chicago Institutional Review Board for research. Ovarian cancer tissue was histologically classified and staged by a pathologist according to tumor-node-metastasis (TMN) and/or International Federation of Gynecology and Obstetrics (FIGO) classifications (Table 1).

METHOD DETAILS

Immunohistochemistry

Ovarian cancer tissues obtained fresh from surgery were fixed overnight in 4% formaldehyde at 4°C. After serial dehydration, the tissues were embedded in paraffin and cut into 5 μm thick sections. Histological evaluation was done with hematoxylin and eosin (H&E). Immunohistochemical staining was performed to confirm the presence of cytokeratin-7 (Thermo Scientific), TOX (ThermoFisher), pan-vimentin (DAKO), CD45 (Agilent), CD4, CD8a, CD68, CD163, CD19 and GNLY (Abcam) positive cells. Briefly, sections were deparaffinized and rehydrated using xylene and serial dilutions of EtOH in distilled water. Tissue sections were incubated in citrate buffer, pH 6 and heated in a microwave oven. Anti-cytokeratin-7 (1:1000), anti-vimentin (1:100), anti-CD45 (1:100), anti-CD4 (1:50), anti-CD19 (1:200), anti-CD8 (1:400), anti-TOX (1:200), anti-CD163 (1:2), anti-CD68 (1:40) and anti-GNLY (1:2000) antibodies were applied on tissue sections for one-hour incubation at room temperature in a humidity-controlled chamber. The antigen-antibody bindings were detected with labeled polymer-HRP Envision system (DAKO, K4007) and DAB+ chromogen (DAKO, K3468) system. Tissue sections were briefly immersed in hematoxylin for counterstaining and covered with cover glasses. We used Imagescope, a digital histopathology software, to annotate and quantify the H&E and IHC staining.

Tissue digestion, red blood cell lysis and dead cell removal

Ovarian tumors were transported in DMEM/F12 containing 10% FBS and 1% P/S (10% DMEMF/12) on ice to the laboratory. The tissue was minced manually with a scalpel and enzymatically digested using 1.5 mg/ml collagenase IV (Sigma-Aldrich), 1 mg/ml hyaluronidase (Sigma-Aldrich) and 500 μg/ml DNase I (GoldBio) in Hank's balanced salt solution (HBSS) in a 37°C shaker (200 rpm) for 0.5 – 2 h. Following digestion, adipocytes were separated from the stromal vascular fraction (SVF) by centrifugation and discarded. Note that the size and density of adipocytes make them unamenable to droplet based single-cell RNA-seq. SVF cells were resuspended in 10% DMEMF/12 and filtered serially through 70 μm and 40 μm strainers. Red blood cells were lysed by incubating the cell pellet in RBC lysis buffer (Miltenyi Biotec, 130-094-183) for 2 minutes. Lysis was quenched by adding excess 10% DMEMF/12. The number of live cells was enriched using the dead cell removal kit (Miltenyi Biotec, 130-090-101) according to manufacturer's instructions.

Drop-seq experiments

Drop-seq experiments were performed as previously described (Macosko et al., 2015). Briefly, cells were loaded at a concentration of 100,000 cells/ml in PBS and 0.01% BSA (NEB, #B9000S) and the barcoded beads (Chemgenes) at 120,000 beads/ml were loaded in Drop-seq lysis buffer consisting of 0.2% Sarkosyl (Teknova, #S3376), 6% Ficoll (Sigma, #F5415-50ml), 0.02 M EDTA (Fisher, #BP2482-500), 0.2 M Tris-HCl pH7.5 (Fisher, #BP1757-500), and 0.05 M DTT (Teknova, #D9750) in water (Invitrogen, #10977-015). Droplets were generated using a 125-micron Drop-seq microfluidic device and inert oil-surfactant mix (BioRad, #1864006) at 16 mL/hr (oil), 4 mL/hr (cells) and 4 mL/hr (beads) with ~15 minutes per collection. Following collection, drops were broken in 50 mL conical tubes using perfluorooctanol (Synquest, #2101-3-20) and spin down at 1000 xg for 1 min. Barcoded beads with mRNA hybridized onto them were collected from the oil-water interface using a 1 mL pipette and transferred to a fresh 50 mL conical tube. The mRNA-bound barcode beads were washed three times in 30 mL of 6x Saline-Sodium Citrate solution (Teknova, #S0282), transferred to a 1.5 mL centrifuge tube and washed once in 500 μL of 1x Maxima H- RT buffer (Thermo, #EP0751). Reverse transcription (RT) was performed on the beads in a modified RT recipe consisting of 1x Maxima H- RT buffer, 4% Ficoll PM-400 (GE Healthcare, #17-0300-05), 3 mM MgCl₂ (Sigma, #M1028), 1 mM Betaine (Sigma, #14300), 1 mM dNTP (Clontech, #639125), 1 U/μL RNase Inhibitor (Lucigen, #F83923), 2.5 μM Template-Switching Oligo (TSO) primer: AAGCAGTGGTATCAACGCAGAGTGAATrGrGrG (IDT), and 10 U/μL Maxima H- RT enzyme (Thermo, #EP0751) in a total volume of 200 μL. RT was performed by a 30-minute incubation at room temperature, followed by a 90-minute incubation at 50°C, both under end-over-end rotation.

Barcoded cDNA attached to the beads or STAMPs were generated by reverse transcription were thoroughly washed (in 0.5% SDS and 0.02% Tween 20 each in Tris-EDTA buffer), treated with 1 U/μL exonuclease I (Fisher, #M0293L), rewashed and the number of STAMPs was counted. 5000 STAMPs were aliquoted per well in a 96-well plate and the cDNA attached to the STAMPs were amplified through 14 PCR cycles using 1x Kapa Hifi Hotstart Mastermix (Fisher, #NC0465187) and 2.5 μM PCR primer: AAGCAGTGGTATCAACGCAGAGT (IDT). Supernatant from each well was pooled and cleaned with 0.6X Ampure beads. Purified cDNA was quantified using Qubit 3.0 (Invitrogen). 450-650 pg of each sample with standard Nextera P7 primer and custom P5-TSO hybrid oligo: AATGA TACGGCGACCACCGAGATCTACACGCCTGTCCGCGGAAGCAGTGGTATCAACGCAGAGT*A*C and were used as input for Nextera library preparation (12 PCR cycles; Illumina, #FC-131-1096). Tagmented libraries were quantified using Agilent BioAnalyzer High Sensitivity chip before submission for sequencing on Illumina's NextSeq 500, using 75 cycle v3 kits. Paired end sequencing

was performed with 20 bp for Read 1 and 64 bp for Read 2 using custom Read 1 primer, GCCTGTCCGCGGAAGC AGTGGTAT CAACGCAGAGTAC and 5% Illumina PhiX Control v3. The data discussed in this publication have been deposited in NCBI's Gene Expression Omnibus <https://www.ncbi.nlm.nih.gov/geo/query/acc.cgi?acc=GSE147082>.

Data processing, alignment and clustering analysis

The ovarian cancer samples from six patient's metastatic omentum were sequenced with Drop-seq. A total of 13 sequencing runs were performed for six Drop-seq samples where each sample was sequenced at least twice (PT-2 was sequenced three times). Each run produced paired-end reads, with Read 1 representing the 12 bp cell barcode and a six bp long unique molecular identifier (UMI) and Read 2 representing a 60–64 bp mRNA fragment. Paired-end reads from the same samples were merged to generate six paired-end fastq files. Read count matrices were generated from sequence reads from the Drop-seq experiments for both exonic and intronic regions in the human genome (gencode hg38 v.27) using a *snakemake* pipeline (Selewa et al., 2019) and STAR version 2.5.3 aligner (Frankish et al., 2019; Dobin et al., 2013). Individual count matrices were produced for each of the six patients after accounting for UMI duplicates.

The summarized counts for each gene were inferred based on both exonic and intronic reads to produce the gene expression matrix per sample. To select high quality cells, we applied a filter based on the number of genes detected per cell. Prior to filtering, each sample produced approximately 5,000 cells. Based on the median number of genes captured, cells with less than 600 genes with detected expression were removed from the datasets (Tables 2 and S1). We followed a standardized pipeline using single cell analysis tool suite, Seurat v3.0.2 (Butler et al., 2018; Stuart et al., 2019). A global-scaling logarithmic normalization method (Stuart et al., 2019) was applied to all samples that normalized the feature expression counts for each cell by the total expression counts, multiplied by a scale factor of 10,000 (TP10K), and transformed the scaled data to log units with a small shift (+1) to handle 0 counts. Each normalized matrix was then scaled by a linear transformation to center the mean gene expression for all cells. The most variable genes were extracted for principal component analysis (PCA). We applied PCA on the normalized expression matrix with the most variable genes to extract the top 50 components in the data, followed by a heuristic 'elbow' plot on the variance explained of each PC. We selected the number of top variant PCs based on the elbow plot which varied from 10 to 20 depending on the sample. The top PCs were used in further exploration of the data, such as UMAP (McInnes et al., 2018) dimension reduction, construction of K-nearest neighbor graphs, shared nearest neighbor modularity optimization-based clustering (Waltman and Eck, 2013), etc. For analysis that included multiple samples, integration through anchoring (Stuart et al., 2019) was applied. A subset of genes, usually highly variable ones, was selected to perform the integration, where the integrated gene expression matrix had a lesser number of features (genes) than the original gene expression matrix. The samples from multiple patients were integrated before classifying cell types. Differential expression analysis was performed through *FindMarkers* function in Seurat using the Wilcoxon Rank Sum test, and statistically significant markers were extracted for sub-populations or contrast groups based on an adjusted p value (adj. p-val.) threshold of 0.05. We used dimension reduction methods, UMAP (McInnes et al., 2018) to generate 2D plots to visualize different cell populations in the experiments.

Cancer subtype classification and correlation with The Cancer Genome Atlas

Four cancer subtypes- differentiated, immunoreactive, mesenchymal, and proliferative were determined from previous bulk sequencing study in ovarian cancer (The Cancer Genome Atlas Research Network, 2011). Modular scores (Tirosh et al., 2016) were generated between gene expression levels for each cell with upregulated marker signatures on the four subtypes. The subtypes were then assigned to individual cells by the highest positive modular score. In the absence of positive modular scores, the subtype was considered undecided.

Cell type classification and correlation with CellAtlas

To assign cell types to individual cells, we used a bulk RNA sequencing data-set from 95 cell lines collected by CellAtlas (Mabbott et al., 2013) that covered 33 major cell types in normal human tissue, including common immune, endothelial, epithelial, fibroblast and mesodermal cells. The cell lines can be further divided into 60 subtypes. We inferred the similarity between individual cells in the samples and cell lines by calculating the pairwise Pearson correlation matrix $C = \{cor(i,j)\}$ between any cell i from the Drop-seq experiments with any cell line, j in the CellAtlas leveraging the R package *dmatch* (Chen et al., 2021). Ward's hierarchical agglomerative clustering was applied on the CellAtlas cell lines to group the cell lines into larger and more general cell type categories. This was done to eliminate any bias in the CellAtlas dataset and remove rare or under-powered cell types. The resulting clusters of cell lines were annotated by the most frequent major cell type from the cell-line groups. For each cell in our tumor samples, cell type was assigned from top five highly correlated major cell type clusters. Ambiguous cell types were collapsed with neighboring cell types, based on expression profiles.

Classification with cluster markers, canonical genes, and genetic functions

We used the cell types obtained from CellAtlas correlation as a baseline and then curated those cell types manually using canonical genes and functional association. Differentially expressed marker genes were extracted from cell clusters. Cross-referencing was done between gene markers and known canonical genes of the cell types. Gene ontology and pathway enrichment was performed on gene markers to provide additional evidence for cell type assignment (Chen et al., 2009). We identified nine major cell types

including: epithelial cells, fibroblast, mesenchymal stem cells (MSC), embryonic stem cells (ESC), endothelial cells and three immune cell types: naive and plasma B cells, T cells, and macrophages.

Gene Ontology (GO) and Pathway analysis sometimes gives general/noisy functional categories which make certain cell types hard to identify. By leveraging prior knowledge from the CellAtlas mapping, we were able to locate the relevant functional categories for those cell types and narrow down their marker genes efficiently (Mabbott et al., 2013). Moreover, by leveraging the consensus of both GO and CellAtlas analysis, we obtained higher confidence in classifying cell types in each patient sample.

Marker identification for subtypes of various cell populations

To explore the cellular subtypes in detail, we analyzed cells belonging to four major clusters by hierarchical clustering strategy. These included the central cluster (containing cancer epithelial cells and ESCs), as well as all three immune sub-populations; T cells, B cells (including plasma cells), and macrophages separated by groups (high T_{inf} and low T_{inf}). The significance of differential gene expression was estimated using the Wilcoxon rank-sum test. We used a cutoff of 0.05 on the adj. p-val. to distinguish the significant markers for each sub-population.

Comparison and validation with bulk sequencing data from The Cancer Genome Atlas (TCGA) program

To compare gene expression levels among *TOX*, *GNLY*, *CD4*, and *CD8* between different ovarian cancer molecular subtypes, we extracted bulk RNA-seq data from 368 serous ovarian cancer patient samples from the TCGA Research Network: <https://www.cancer.gov/about-nci/organization/ccg/research/structural-genomics/tcga>. The bulk RNA-seq gene expression matrix included 56,431 transcripts and 368 samples associated with 25 batches. We performed log normalization on expression counts, scaling of centered expressions, and regressed out batch variable from the scaled expression data. Four subtypes- differentiated, immuno-reactive, mesenchymal, and proliferative were assigned to each sample. The correlations were measured using the Pearson method for all four subtypes between the two gene-pairs: *TOX/CD8* and *GNLY/CD4*. Statistical significance for each correlation was estimated based on a t-distribution with n-2 degrees of freedom where n is the number of samples per cancer subtype. The significance was determined by a p value cutoff of 0.05.

QUANTIFICATION AND STATISTICAL ANALYSIS

IHC staining images were analyzed and quantified using Aperio ImageScope [v12.4.05043]. Statistical analysis is summarized in figure legends. Correlation between area of adipocytes and vimentin, CK-7 and CD45 was assessed in Prism 9 (GraphPad; 8.4.3) by one-way ANOVA.